Laser & Photonics Reviews

LASER & PHOTONICS REVIEWS

www.lpr-journal.org

RESEARCH ARTICLE OPEN ACCESS

Activation and Detection of Forbidden Low-Frequency Raman Modes in MoS_2 by Near-Field Gradient Illumination

Zhen Zong[1] | Ryosuke Morisaki[1] | Kanami Sugiyama[2] | Masahiro Higashi[3] | Takayuki Umakoshi[1] | Prabhat Verma[1]

[1]Department of Applied Physics, The University of Osaka, Osaka, Japan | [2]Department of Molecular Engineering, Kyoto University, Kyoto, Japan | [3]Department of Complex Systems Science, Nagoya University, Nagoya, Japan

Correspondence: Prabhat Verma (verma@ap.eng.osaka-u.ac.jp)

Received: 7 February 2026 | **Revised:** 30 March 2026 | **Accepted:** 25 June 2026

Keywords: forbidden Raman modes | low-frequency Raman modes | near-field gradient | plasmon-enhanced Raman scattering | plasmonics

ABSTRACT

Interlayer coupling in two-dimensional (2D) materials is governed by weak van der Waals forces, resulting in low-frequency (LF) vibrations in Raman scattering. These LF-phonons provide direct insights into interlayer interactions, stacking configurations, and defects; however, many of these modes are inaccessible in conventional Raman spectroscopy due to symmetry-based selection rules, leading to a loss of critical structural information. Here, we demonstrate that plasmonic near-field gradients can relax Raman selection rules and enable the activation of forbidden LF phonons. Using silver-nanoparticle-decorated 3-layer MoS_2 as a model system, we experimentally activated and detected forbidden LF-phonons, namely the E" and A_2" modes. Combining Raman imaging with density functional theory and electromagnetic simulations, we demonstrate that activation is mainly governed by the local near-field gradient, and it occurs only when the near-field gradient aligns with the phonon vibration direction. This work reveals a near-field-gradient mechanism for accessing Raman-forbidden interlayer phonons and offers a framework for probing hidden vibrations, symmetry breaking, and interlayer interactions in 2D materials.

1 | Introduction

Raman spectroscopy is one of the most powerful techniques for probing the structural and vibrational properties of materials [1]. However, many vibrational modes cannot be observed in conventional Raman spectra due to restrictions imposed by the Raman selection rules [2]. These Raman-forbidden modes conceal important structural information within the material system. This issue is particularly significant for two-dimensional (2D) materials, where low-frequency Raman modes arising from interlayer vibrations directly reflect key van der Waals interlayer properties, such as interlayer coupling, stacking configuration, and symmetry [3–22]. With the exception of the shear and breathing modes, all other low-frequency interlayer vibrations are entirely prohibited from appearing in conventional Raman spectra by the selection rules [23, 24]. At the same time, low-frequency Raman modes are very weak and lie close to intense Rayleigh scattering, making their high-sensitivity detection challenging.

To date, there have been no reports of high-sensitivity detection and imaging of low-frequency Raman-forbidden modes. Activating such modes in an optical experiment requires overcoming the momentum-conservation constraint imposed by the selection rules, which require that Raman scattering satisfy both energy and momentum conservation. However, the momentum carried by an incident photon is insufficient to excite certain phonons, and hence they remain unexcited. Therefore, a local symmetry-breaking must be introduced to alter the electromagnetic fields locally and activate the forbidden modes. Breaking the local symmetry relaxes the conservation laws by allowing additional

wavevector components to participate in the light–matter interaction, which effectively provides the extra momentum required to couple to phonons that are otherwise forbidden. Therefore, Raman-forbidden modes can be activated through symmetry-breaking mechanisms, such as local physical deformation or highly nonuniform electromagnetic fields with strong spatial gradients.

Plasmonic resonance that creates a highly localized, strong-gradient electromagnetic field offers a promising solution to this challenge [18, 25–52]. Under certain conditions, metallic nanoparticles generate strong near-field gradients with rapid spatial variation and effective momentum components far exceeding those of free-space photons. These steep near-field gradients can break local symmetry and provide the additional optical momentum required to activate phonons that are forbidden by the selection rules [2, 24, 53–62]. Meanwhile, the plasmonic near field also enhances the weak low-frequency Raman signals, allowing them to be distinguished from background signals.

Guided by this principle, we built a low-frequency plasmon-enhanced Raman spectroscopy (LF-PERS) system capable of stably acquiring enhanced Raman signals down to about 10 cm^{-1} and activating Raman-forbidden modes through near-field gradients. Using 3-layered MoS_2 as a model system, we experimentally activated and visualized two kinds of low-frequency forbidden interlayer phonons, namely the E'' and A_2'' modes, at the same time. Since monolayered MoS_2 does not have interlayer interactions and 2-layered MoS_2 has only two low-frequency vibrations, which are the breathing and the shear vibration modes, we selected a 3-layered sample, which has additional vibrations that are Raman-forbidden. Combined with density functional theory (DFT) calculations and Raman imaging, we confirmed that these forbidden modes are intrinsic vibrational modes of the material and can only be excited within the plasmonic near-field region of the nanoparticles, where a strong field gradient is present. Our DFT results indicate that local physical deformation at the MoS_2-Ag interface can contribute to the activation of Raman-forbidden modes by weakly breaking the lattice symmetry. Recent studies have shown that local strain can also give rise to new low-frequency vibrational modes in 2D materials [52]. In contrast, the modes investigated in this work are intrinsic Raman-forbidden phonons that become accessible through near-field gradients induced relaxation of selection rules. By systematically analyzing nanoparticle size, near-field gradient variations, and normalized forbidden mode intensities, we uncovered the physical mechanism underlying forbidden mode activation and discovered that strong localized near-field gradients play a central role in providing the additional optical momentum and determining the activation efficiency, while small interfacial physical deformation serves only as a minor symmetry-relaxation factor. Furthermore, the activation efficiency exhibits clear directionality, and activation occurs effectively only when the near-field gradient direction matches the phonon vibration direction.

This study not only enables the experimental detection of hidden interlayer phonons in 2D materials but also establishes a new plasmonic near-field–based paradigm for probing forbidden vibrations, interlayer coupling, and symmetry breaking, opening new possibilities for characterizing 2D materials and van der Waals heterostructures.

2 | Results and Discussion

We first prepared large-area, few-layered MoS_2 flakes using the gold-mediated exfoliation method and transferred them onto SiO_2 glass substrates that had been thoroughly cleaned using a piranha solution [3, 42, 63, 64]. A solution containing silver nanoparticles of average size 80 nm (Sigma-Aldrich 730777) was then spin-coated onto the MoS_2 surface to ensure that the particles were well-distributed, avoiding any large aggregation. It is important to note that individual nanoparticles differ slightly in size and shape.

To detect low-frequency Raman signals down to 10 cm^{-1}, we built an LF-Raman system, as shown in Figure 1a. Edge filters and notch filters used to block Rayleigh scattering in a conventional Raman setup transmit only Raman shifts above approximately 100 cm^{-1}, and therefore, a conventional Raman is unable to measure low-frequency Raman scattering. To overcome this limitation, we used a set of ultra-narrow Bragg volume notch filters (BNFs) with a spectral bandwidth of approximately 8 cm^{-1} [65]. The basic function of a BNF is to reflect a particular wavelength, with a narrow linewidth, at a certain angle. One BNF was placed in the excitation path at such an angle so that it allowed 532 nm wavelength to follow the excitation path to narrow the linewidth of the 532 nm laser to approximately 8 cm^{-1}, while three additional BNFs were cascaded in the detection path with different angles so that they rejected selectively the Rayleigh light (532 nm) by reflecting it away from the detection path, effectively blocking Rayleigh scattering almost completely while allowing a complete transmission of Raman scattered light. Since our experiment relies on PERS, we introduced a z-polarizer (a combination of radial polarizers) into the optical path to selectively illuminate silver nanoparticles in the z-direction and effectively enhance the near-field intensity at the silver nanoparticle-MoS_2 interface, as shown in the inset of Figure 1a. Under dominant z-polarization, the focused beam produces a strong out-of-plane near-field component, significantly enhancing Raman sensitivity at the nanoparticle-sample interface [66, 67]. Details of the optical configuration are provided in Section S1. With this optical configuration, we can obtain stable and reliable LF-PERS signals down to 10 cm^{-1}.

Using the LF-PERS system, we first evaluated its capability for LF-PERS detection. Figure 1b,c shows the low-frequency (below 50 cm^{-1}) and high-frequency (above 260 cm^{-1}) Raman spectra of 2-layered and 3-layered MoS_2 samples, respectively. In each figure, the black spectra marked by 1 represent the unenhanced signal, measured away from silver nanoparticles, and the red spectra marked by 2 and 3 represent the enhanced signals obtained right below a silver nanoparticle under PERS configurations. Two red spectra were measured from two different locations under two different silver nanoparticles. For 2-layered MoS_2 (Figure 1b), the low-frequency region contains the interlayer shear mode at 23 cm^{-1} and the breathing mode at 40 cm^{-1}, while the high-frequency region includes the E_{2g} mode at 380 cm^{-1} and the A_{1g} mode at 399 cm^{-1}. When enhanced at locations directly below a nanoparticle, all Raman peaks increase significantly in intensity. The out-of-plane breathing and A_{1g} modes display stronger enhancement than the in-plane shear and E_{2g} modes, which is attributed to the strong vertically polarized near-field light generated under z-polarized excitation. In addition, a new Raman peak appears at approximately 280 cm^{-1} in the enhanced

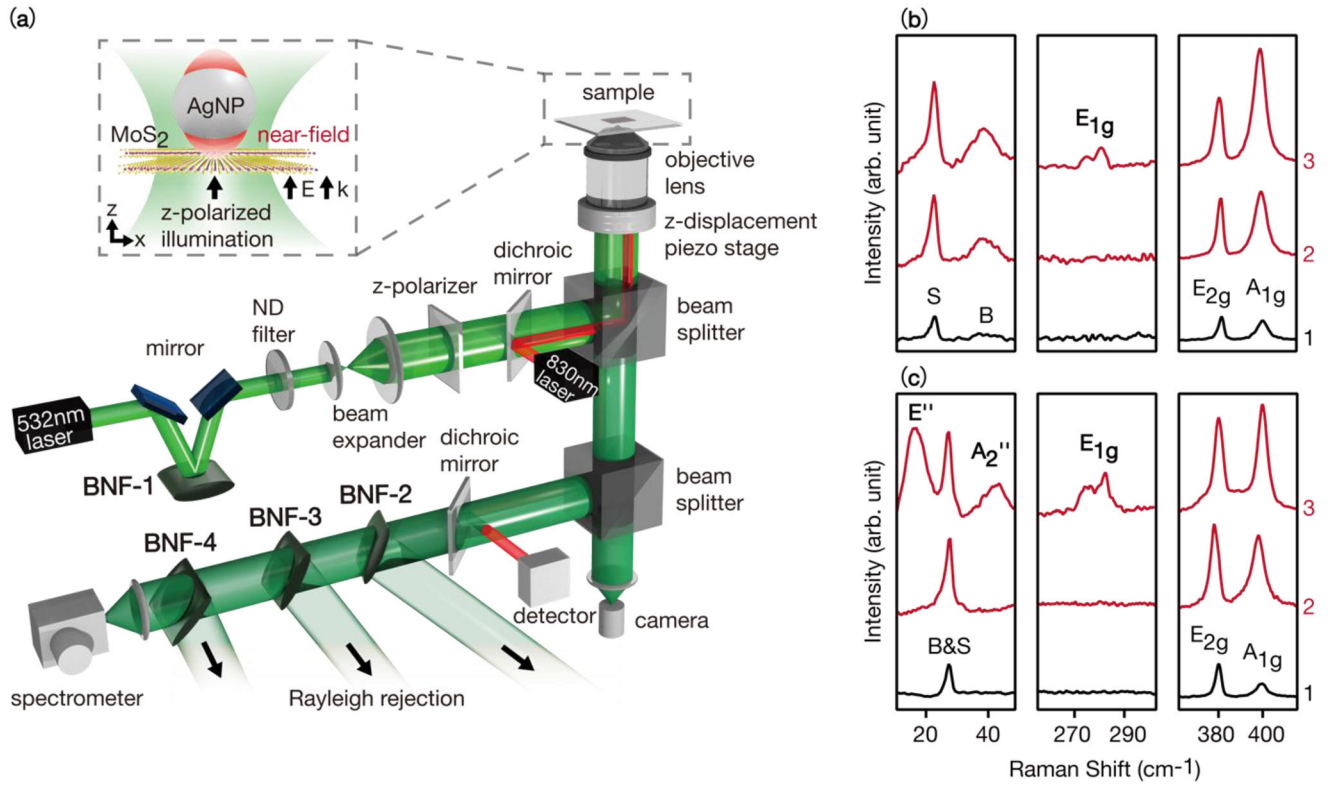

FIGURE 1 | (a) LF-PERS system. Raman spectra of (b) a 2-layered and (c) a 3-layered MoS_2 sample. Black and red curves are unenhanced spectra measured away from a silver nanoparticle and enhanced spectra measured directly below a silver nanoparticle, respectively. Raman peaks marked by S and B correspond to the low-frequency shear-mode and the breathing-mode, respectively, and E_{2g} and A_{1g} correspond to the high-frequency in-plane and out-of-plane vibrational modes, respectively. E'', A_2'' represent low-frequency Raman-forbidden modes, and E_{1g} is the high-frequency Raman-forbidden mode.

high-frequency spectrum 3. This peak, which is not observed in spectrum 2, corresponds to the E_{1g} vibrational mode, which is forbidden according to Raman selection rules, showing that the high-frequency forbidden mode is activated under one of the two silver nanoparticles. In the low-frequency region of 2-layered MoS_2, only one shear mode and one breathing mode exist; therefore, no low-frequency forbidden modes appear, serving as a reference. When the number of layers increases from 2 to 3 (Figure 1c), the interlayer vibrational modes exhibit clear changes, where the breathing mode redshifts and the shear mode blueshifts, and the two modes overlap near 27 cm^{-1}. The high-frequency E_{2g} and A_{1g} peaks also shift slightly to 379 cm^{-1} and 400 cm^{-1}, respectively, consistent with the layer-dependent Raman shifts observed in few-layered MoS_2 samples (see Section S2 for detailed spectra). More importantly, the enhanced 3-layered spectra measured at locations directly under silver nanoparticles exhibit not only the same high-frequency forbidden E_{1g} peak in spectrum 3 but also two interlayer modes that do not exist in 2-layered MoS_2 in the low-frequency region, a peak at 15 cm^{-1} and another at 42 cm^{-1}. By comparing with the unenhanced spectrum, we confirm that both peaks arise from low-frequency interlayer shear E'' and interlayer breathing A_2'' modes that are forbidden in conventional Raman scattering of 3-layered MoS_2. These forbidden Raman modes are not observed in spectrum 2. Here, we emphasize that not all silver nanoparticles are able to activate the forbidden modes, as evidenced by spectra 2 and 3 for both 2- and 3-layered samples. This work demonstrates the activation of low-frequency forbidden interlayer Raman modes in MoS_2 using PERS, where certain silver nanoparticles are able to activate them. In the following discussion, we selectively used only those particles that show forbidden modes.

To further verify that the additional Raman peaks observed in our experiments indeed correspond to Raman-forbidden vibrational modes, and to establish the correspondence between the experimental Raman features and intrinsic phonon modes, we performed DFT calculations using CRYSTAL23 with the local density approximation (LDA, SVWN exchange–correlation functional) and the two-dimensional periodic boundary condition [68]. The HAYWSC-311(d31)G, DURAND-31G*, and HAYWSC-311d31G basis sets were used for Mo, S, and Ag atoms, respectively [69–71]. We first analyzed the intrinsic vibrational modes of 3-layered MoS_2. As shown in Figure 2a, seven intrinsic vibrational modes of 3-layered MoS_2 were identified, and their corresponding vibration directions were specifically determined. Among them, E'' and S are the interlayer shear vibrations, B and A_2'' are the interlayer breathing vibrations, E_{1g} and E_{2g} are the in-plane intralayer vibrations, and A_{1g} is the out-of-plane intralayer vibration.

We then calculated the intrinsic Raman spectrum of 3-layered MoS_2 to identify which intrinsic vibrational modes are Raman-active (black spectra in Figure 2b). The calculated phonon frequencies show that the S modes appear at 32 cm^{-1}, the B modes at 38 cm^{-1}, the E_{2g} mode at 390 cm^{-1}, and the A_{1g} mode at 412 cm^{-1}, respectively. As expected, the forbidden modes do not

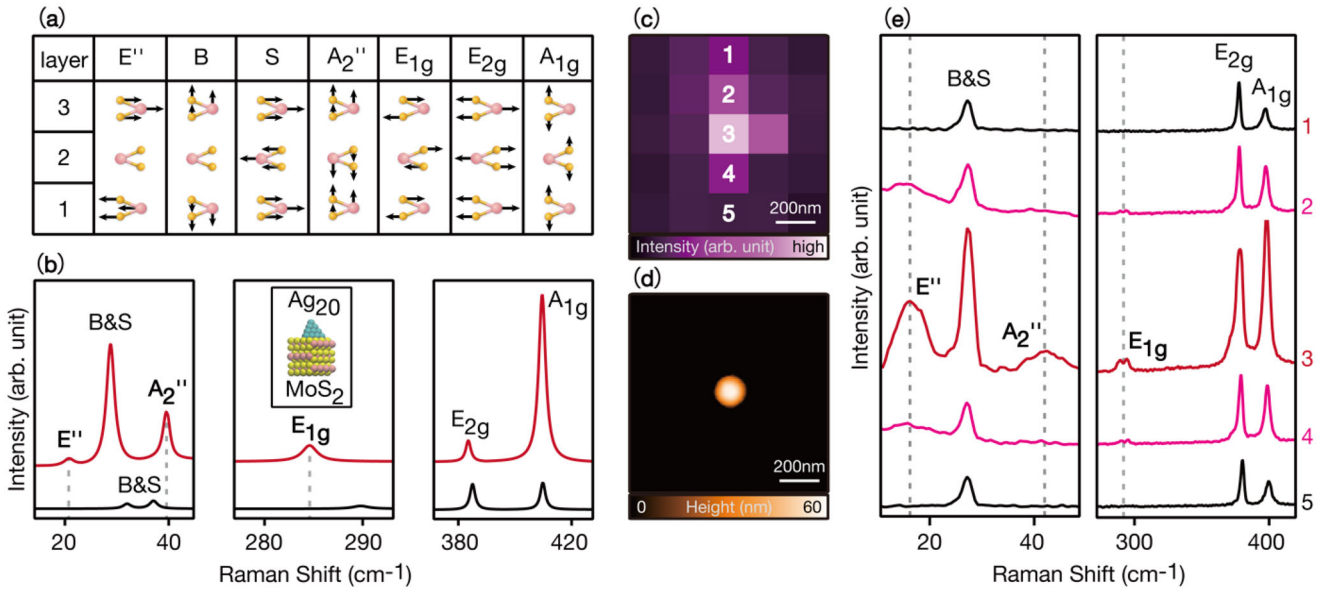

FIGURE 2 | (a) Intrinsic vibrational modes of a 3-layered MoS_2 sample, where the three layers are indicated by the numbers 1, 2, and 3. (b) Raman spectra of 3-layered MoS_2 from DFT calculation. The black and red curves represent unenhanced and chemically enhanced spectra, respectively. In enhanced Raman spectra, peaks corresponding to Ag vibrations were present but were omitted for clarity. (c) A Raman intensity image at 27 cm^{-1} shared by both low-frequency shear and breathing modes for a 3-layered MoS_2. (d) An AFM image at the same position as (c). (e) Spectra collected at different positions marked in (c).

appear in these spectra because their symmetries do not satisfy the Raman selection rules. The experimental Raman-active peak near 27 cm^{-1} is attributed to the combined S and B interlayer modes that coincide for 3-layered MoS_2, the peak near 379 cm^{-1} to the E_{2g} in-plane intralayer mode, and the peak near 400 cm^{-1} to the A_{1g} out-of-plane intralayer mode. The calculated vibrational frequencies exhibit a blueshift relative to the experimental values, which arises from the overbinding tendency of LDA, which increases the force constants in the DFT calculation [72–74]. This provides a reference for assigning the experimentally observed Raman peaks.

After identifying Raman-active modes, we next determined which other intrinsic vibrational modes are Raman-forbidden and can only be activated when the symmetry is broken. Since an easy way to introduce symmetry breaking in DFT calculations is through physical contact deformation, we placed a silver nanocluster composed of 20 silver atoms on top of a 4 × 4 × 1 supercell of 3-layered MoS_2 (model shown in the inset of Figure 2b) and recalculated the Raman spectrum of the combined system (red curves in Figure 2b). It is important to note that the conventional DFT calculations do not include plasmonic near-field effects and therefore cannot account for the strong electromagnetic field gradients generated by metallic nanoparticles under resonant excitation. In the present simulations, only local physical deformation at the MoS_2-Ag interface and chemical enhancement arising from charge transfer are explicitly included. However, this is sufficient to identify forbidden Raman modes through simulation. The calculated phonon frequencies show that the E" mode appears at 20 cm^{-1}, the B and S modes near 30 cm^{-1}, the A_2" mode at 40 cm^{-1}, the E_{1g} mode at 285 cm^{-1}, the E_{2g} mode at 388 cm^{-1}, and the A_{1g} mode at 410 cm^{-1}, respectively. Compared with the intrinsic modes, a redshift of the phonon frequencies by a few wavenumbers is observed upon introducing the Ag nanocluster. These frequency shifts arise from the interaction between MoS_2 and the silver nanocluster, which slightly modifies the interatomic force constants. Under this configuration, all three forbidden modes E", A_2", and E_{1g} appearing in the calculated spectrum reproduce the forbidden peaks observed in the experiment. Based on the appearance of these modes in the symmetry-broken DFT spectrum and their vibrational characters identified above, the experimental peak near 15 cm^{-1} is attributed to the E" interlayer shear mode, the peak near 42 cm^{-1} to the A_2" interlayer breathing mode, and the peak near 280 cm^{-1} to the E_{1g} intralayer mode. The emergence of forbidden modes in the simulation arises primarily from local physical deformation at the MoS_2-Ag interface that breaks symmetry, together with chemical enhancement induced by charge transfer. Although the symmetry breaking introduced in the DFT model is weak, it is sufficient to break the Raman selection rules and allow the forbidden modes to become Raman active. It should be noted that the mechanism of symmetry breaking in the DFT model differs from that in the experiment shown in Figure 1b,c. Here, DFT calculations help to identify the intrinsic vibrational modes corresponding to the experimentally observed forbidden peaks, while the detailed activation mechanism in the experiment, particularly the role of the plasmonic near-field gradient, is discussed in subsequent sections.

After confirming the existence of the forbidden modes and their vibrational properties through DFT calculations, we further examined whether their activation in the experiment indeed originates from the silver nanoparticles. To this end, we performed spatial Raman mapping around an isolated silver nanoparticle to analyze the spatial mapping and activation behavior of the forbidden modes. Figure 2c shows a Raman intensity image of the low-frequency mode at 27 cm^{-1}, which is a combination of the shear and breathing modes, with a scanning step of 200 nm. The

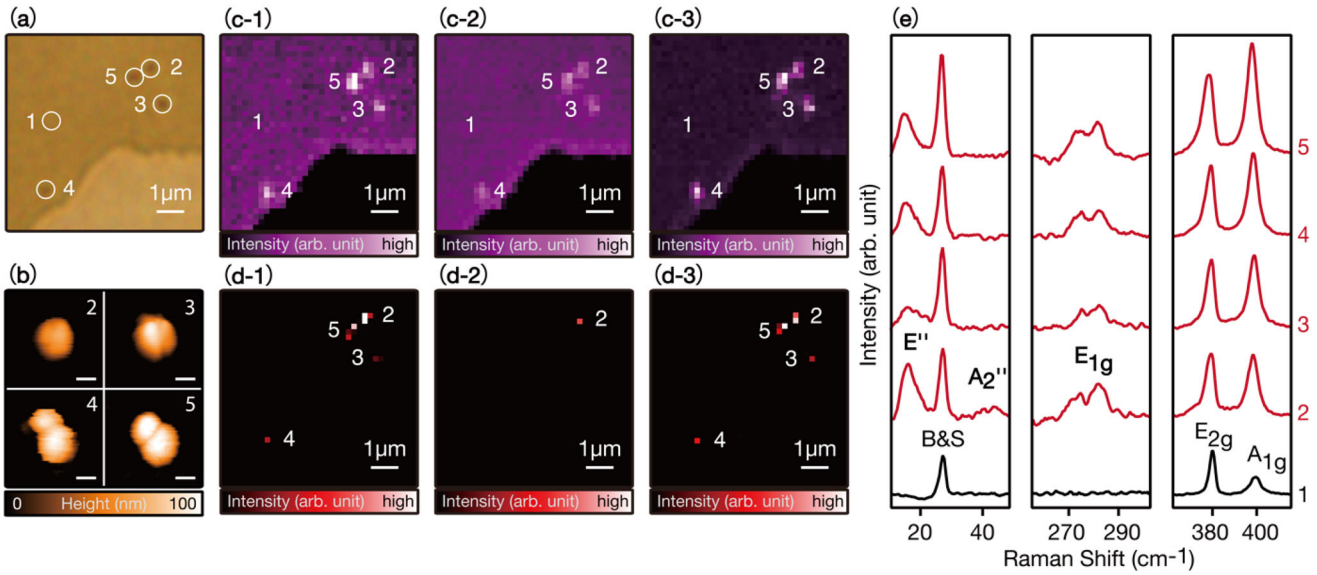

FIGURE 3 | (a) An optical image of a 3-layered MoS_2 sample. (b) A collection of four different AFM images obtained from locations marked from 2 through 5 in (a), showing the existence of silver nanoparticles at these locations. Scale bar: 50 nm. (c-1)–(c-3) Raman intensity images constructed with Raman-active modes: (c-1) shear and breathing modes, (c-2) E_{2g} mode, and (c-3) A_{1g} mode. (d-1)–(d-3) Raman intensity images constructed with Raman-forbidden modes: (d-1) E" mode, (d-2) A_2" mode, and (d-3) E_{1g} mode. (e) Spectra collected at different positions marked in (a). The position marked as 1 corresponds to a region without a silver nanoparticle, and hence shows unenhanced Raman scattering.

bright central region corresponds to the position of an isolated silver nanoparticle. An atomic force microscopy (AFM) image in Figure 2d, obtained from the same location, confirms that this bright spot is an isolated silver nanoparticle. To further illustrate how the Raman signals change spatially, Figure 2e presents spectra collected at different positions marked 1 through 5 in Figure 2c. The results clearly show that all Raman-forbidden modes E", A_2", and E_{1g} appear only in the vicinity of the nanoparticle where the near-field gradient is strong. At the center of the silver nanoparticle, both the Raman enhancement and the forbidden mode intensities are the strongest. At one-pixel away from the nanoparticle, only very weak Raman enhancement remains, and the forbidden modes become nearly invisible. At a two-pixel distance, both Raman enhancement and all forbidden modes completely disappear. These observations verify that Raman-forbidden modes are activated exclusively within the nanoparticle region.

After establishing the activation of forbidden modes by isolated silver nanoparticles, we proceeded to establish if near-field gradient or the physical deformation was the dominant cause for the forbidden-mode activation and performed large-area Raman imaging to investigate whether different silver nanoparticles exhibit consistent activation behavior. Figure 3a shows an optical image of a 3-layered MoS_2 region, where the upper mildly darker area corresponds to MoS_2 flakes and the dark spots marked 2–5 represent silver nanoparticles deposited on the sample. The region marked 1 contains no nanoparticles and serves as a reference. The AFM image in Figure 3b identifies the number and sizes of the nanoparticles, where particles 2 and 3 are single isolated silver nanoparticles, and particles 4 and 5 are dimers. Here, it should be noted that dimer assemblies can have two nanoparticles arranged in any direction. However, in our experiments, we selected only those dimers in which the two nanoparticles were found in the same plane as the sample, meaning the dimer assembly had the same height as the individual nanoparticles. This was important because we used near-field illumination as well as the field gradient in the z-direction (along the height of the nanoparticles). The plasmon resonance in the z-direction was minimally affected by the number of particles, because the height remained the same for both the isolated nanoparticle and the dimer. We confirmed this with COMSOL simulations, which showed only a minor shift of less than 5 nm in the plasmon resonance, negligible compared to the plasmon resonance line width. Figure 3c-1–c-3 shows Raman intensity images constructed with the Raman-active shear and breathing modes, the E_{2g} mode, and the A_{1g} mode, respectively. The brighter, upper regions in these figures indicate the location of the MoS_2 sample via different Raman modes, which correspond to the optical image in Figure 3a. All silver nanoparticles exhibit clear enhancement of the Raman-active modes, indicating that they effectively enhance the local near-field intensity. As expected, region 1 (without silver nanoparticle) shows no enhancement. Figure 3d-1–d-3 shows Raman intensity images constructed with the Raman-forbidden E" mode, the A_2" mode, and the E_{1g} mode, respectively. While Raman-active modes enable clear visualization of the sample in the upper brighter areas in Figure 3c-1–c-3, Raman-forbidden modes are confined to the vicinity of silver nanoparticles and therefore do not reproduce the sample morphology similar to that in Figure 3a. However, we found that not all nanoparticles activate all forbidden modes. For example, the A_2" mode is only activated by particle 2, while it remains absent or extremely weak for the other nanoparticles. This difference is further shown in Figure 3e, which presents Raman spectra collected at the reference region 1 and at the centers of positions 2–4. For Raman-active modes, the enhancement strength increases with the number of nanoparticles. Dimer 5 shows the strongest enhancement, followed by dimer 4, and

finally the isolated silver particles 3 and 2. Between the two isolated silver nanoparticles, particle 3 shows slightly stronger enhancement than particle 2. However, the forbidden modes behave differently: only particle 2 activates the A_2'' mode, and its E'' and E_{1g} intensities are also the strongest among all four particles. In contrast, isolated silver particle 3, despite exhibiting stronger overall enhancement than particle 2, shows almost no activation of A_2'' and the weaker E'' and E_{1g} signals. The forbidden mode intensities of the dimers fall between those of the two isolated silver nanoparticles, but neither activates A_2''. These results demonstrate that the activation of Raman-forbidden modes is highly selective. Their intensities do not scale with the number of nanoparticles or the enhancement strength. Increasing the nanoparticle size or forming dimers increases the contact area and thus the local physical deformation. It also leads to higher near-field intensity, resulting in greater enhancement of Raman-active modes. If physical deformation were the dominant mechanism, larger nanoparticles or dimers would be expected to generate stronger signals from Raman-forbidden modes. However, the experimental results reveal a different trend: despite stronger enhancement and potentially larger deformation, the forbidden modes become weaker or remain completely inactive. This discrepancy indicates that physical deformation is not the primary factor in activating Raman-forbidden modes. In contrast, while the near-field intensity increases with increasing particle size, the near-field gradient decreases, showing that the near-field gradient plays the dominant role. The activation instead depends on the local near-field gradient provided by each nanoparticle and on the alignment between the field-gradient direction and the phonon vibration. Even nanoparticles that generate strong near-field intensity may fail to activate forbidden modes if their near-field gradient is insufficient.

Building on the link between forbidden mode activation and the near-field gradient, we next analyzed a series of isolated silver nanoparticles to quantitatively assess this dependence. Raman-active modes are enhanced by the near-field intensity, while the Raman-forbidden modes that are driven by the near-field gradient are also enhanced by the same near-field intensity. To remove the influence of near-field enhancement and analyze the contribution of the near-field gradient, we normalized the forbidden-mode intensities using the intensities of Raman-active modes measured at the same position. This allows the forbidden mode to more clearly reflect the influence of the near-field gradient. Figure 4a shows the normalized Raman spectra of the forbidden modes E'', A_2'', E_{1g} for silver nanoparticles of different sizes, and Figure 4b presents AFM images of corresponding nanoparticles. Specifically, the intensities of E'' and E_{1g} modes are normalized by dividing their peak intensities by the intensity of the E_{2g} mode, while the A_2'' intensity is normalized by dividing by the A_{1g} mode. This is determined by the relative orientation between the phonon vibration direction and the polarization of the plasmonic near field. Different vibrational modes involve atomic motions either in the in-plane (E'', E_{1g}, and E_{2g}) or out-of-plane (A_2'' and A_{1g}) directions, and their enhancement depends on how efficiently these vibrations couple to the local near-field. Under dominant z-polarized excitation, the plasmonic near field exhibits a strongly anisotropic field distribution. As a result, out-of-plane vibrational modes whose displacement directions are better aligned with the near-field polarization experience more efficient coupling and stronger enhancement. In contrast, in-plane modes with poorer directional matching show weaker enhancement. Therefore, normalizing Raman-forbidden modes with Raman-active modes in the same vibration direction gives a more intuitive measure of how the near-field gradient in the corresponding direction contributes to the forbidden-mode activation. The spectra in Figure 4a are arranged from top to bottom in increasing particle size. The normalized intensities show that forbidden-mode activation is governed by the near-field gradient, which is primarily determined by nanoparticle size. Smaller nanoparticles have higher curvature and therefore generate stronger near-field gradients, making them more effective at activating forbidden modes. On the other hand, larger nanoparticles with lower curvature produce weaker gradients, leading to reduced forbidden-mode activation. A more detailed analysis shows that forbidden modes with different vibration directions do not respond equally to nanoparticle size. This arises from the directional mismatch between the phonon vibration direction and the near-field gradient direction. In our system, the nanoparticles are not perfectly uniform and their lateral (x-y plane) and vertical (z-direction) dimensions vary differently, which leads to anisotropic variations in the near-field gradient. For the in-plane vibrational modes E'' and E_{1g}, the normalized intensities decrease with increasing nanoparticle size, reflecting the decrease in the lateral near-field gradient with increasing size. For the out-of-plane vibrational mode A_2'', the normalized intensity decreases with increasing nanoparticle height, corresponding to a decrease in the vertical near-field gradient. These relationships are clearly seen in Figure 4c,d, where E'' and E_{1g} intensities are plotted against the average diameter in the x-y plane, and the A_2'' intensity is plotted against the nanoparticle height. It should be noted that lateral size measurements are convoluted with the radius of the AFM tip, resulting in larger lateral average diameters. To eliminate this influence, first, the same AFM tip was used for all measurements to ensure consistent comparison, and then the actual diameter was deconvoluted by accounting for the estimated tip radius, providing a close approximation to the true nanoparticle size. Furthermore, the field gradient results from the overall shape of the nanoparticle, which, in experiments, can be affected by any deviation from an ideal spherical shape. To reduce the impact of this nonuniformity, we measured both the major and minor diameters from AFM images and used the average diameter for each nanoparticle. The nanoparticles used in this study have only slight differences between their major and minor diameters; therefore, using an average lateral diameter offers a reasonable estimate of nanoparticle size. Simple fittings in Figure 4c,d, shows quantitative relationships between nanoparticle size and normalized intensity of the forbidden modes along the corresponding vibration direction. As the lateral diameter increases, the lateral near-field gradient and the normalized E'', E_{1g} intensities decrease. Likewise, as the vertical height increases, the vertical near-field gradient and normalized A_2'' intensity both decrease. Furthermore, the normalized intensity of E'' is higher than that of E_{1g}, showing that E'' symmetric vibrations couple more efficiently to the horizontal near-field gradient as compared to the antisymmetric E_{1g} vibrations (Figure 2a).

To further verify that the size dependence of forbidden-mode activation indeed originates dominantly from the near-field gradient rather than from other effects, we performed electromagnetic simulations with COMSOL using the finite element method to analyze the near-field distributions of silver nanoparticles

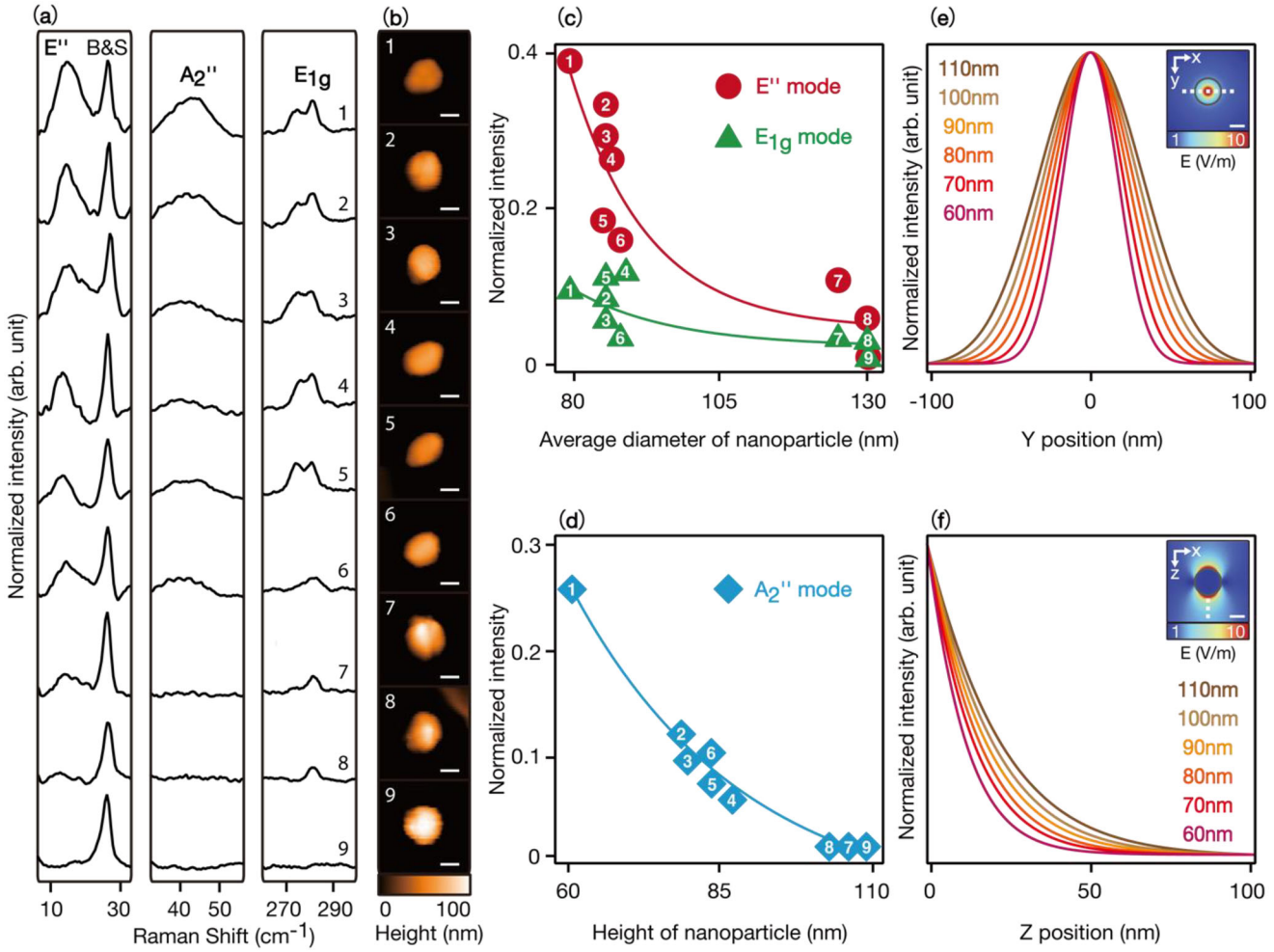

FIGURE 4 | (a) Normalized Raman spectra of a 3-layered MoS_2 sample. (b) AFM images of the corresponding nanoparticles in (a). Scale bar: 50 nm. (c) Normalized intensities of E'' and E_{1g} modes against the average diameter of the nanoparticles. (d) Normalized intensities of A_2'' mode against the height of the nanoparticles. (e) Normalized intensity profiles of the nanoparticles with different sizes along the white dotted line in the inset, which shows a sectional view of the electric field intensity at the interfacial lateral plane between the sample and the nanoparticle. Scale bar: 50 nm. (f) Normalized intensity profile of different-sized nanoparticles along the white dotted line in the inset, which shows a sectional view of the electric field intensity at the vertical central cross-section of the nanoparticle. Scale bar: 50 nm.

of different sizes. In the simulation, we adopted the same z-polarized excitation used in the experiment. To approximate the focused field distribution produced by radial polarization under a high-NA (1.45) objective lens, as in the experiment, four linearly polarized plane waves with the maximum incident angle were introduced from four quadrants and vectorially superimposed to reconstruct an equivalent strong out-of-plane electric field component. This method effectively reproduces the near-field distribution formed by z-polarized illumination in the experiment. Considering that the lateral size measured by AFM may still have some broadening due to the convolution with the AFM tip apex radius, we used the nanoparticle height as the reference and simulated spherical silver nanoparticles with diameters ranging from 60 to 110 nm to match the vertical dimension of the experimental particles. Figure 4e shows the normalized intensity profile of the lateral near-field component extracted along the white dotted line (inset of Figure 4e) in the contact plane between the sample and the nanoparticle, and the corresponding near-field distribution of an 80 nm nanoparticle is displayed in the inset. Figure 4f shows the normalized intensity of the vertical field component along the white dotted line (inset of Figure 4f) in the central cross-section of the nanoparticle, together with its spatial field distribution shown in the inset. The simulations clearly reveal that as the nanoparticle size increases, the near-field gradient at the particle-sample interface decreases, and the rate of gradient decay becomes slower. Importantly, this size-dependent trend agrees well with the experimental behavior of the normalized forbidden mode intensities shown in Figure 4c,d. These simulation results further support the conclusion that forbidden-mode activation is dominated by the near-field gradient rather than by physical deformation. Combining the simulation results with the experimental imaging results, we can establish a clear mechanism whereby forbidden-mode activation requires sufficiently strong local near-field gradients that are also aligned with the phonon vibration direction. Since the near-field gradient is primarily determined by nanoparticle size, it becomes the key factor governing the activation and strength of forbidden Raman modes.

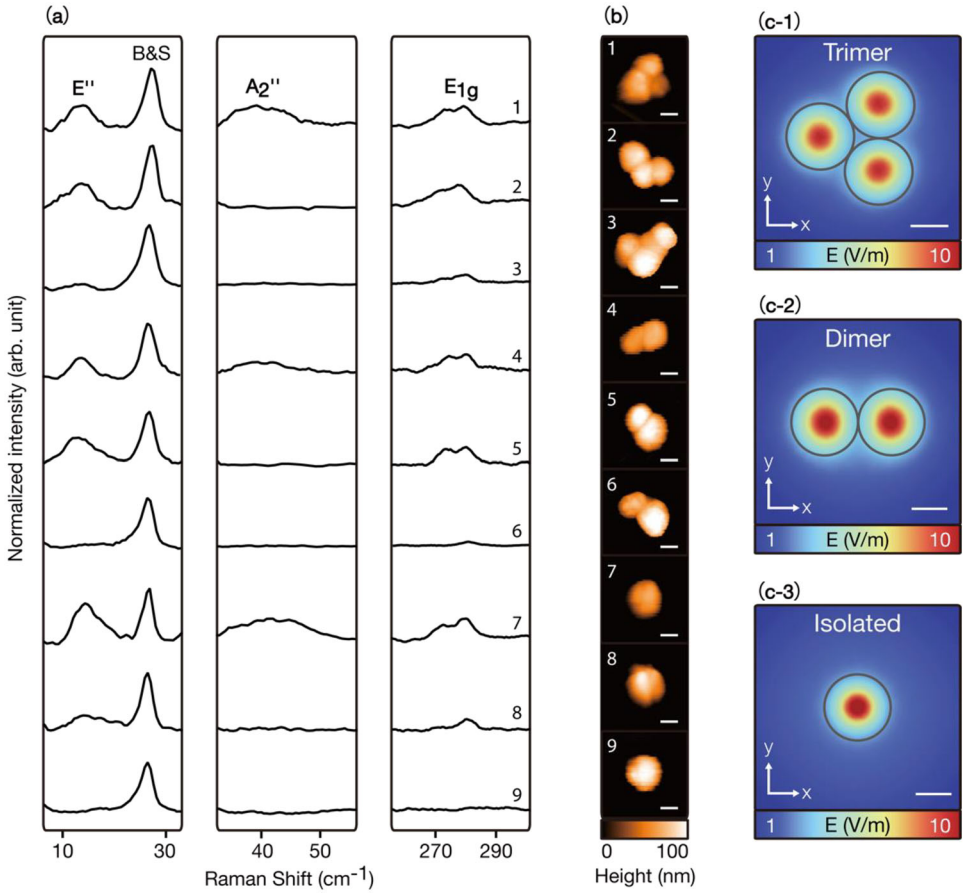

FIGURE 5 | (a) Normalized Raman spectra of a 3-layered MoS_2 sample. (b) AFM images of the corresponding nanoparticles in (a). Scale bar: 50 nm. (c-1), (c-2), (c-3) The electric distributions in the interfacial lateral plane at the contact point between the sample and the nanoparticles of trimer, dimer, and isolated nanoparticle, respectively. Scale bar: 50 nm.

After establishing that the near-field gradient, primarily arising from nanoparticle size, governs forbidden-mode activation in isolated silver nanoparticles, we further examined whether this mechanism also applies to more complex multimeric nanoparticle structures, such as dimers and trimers. Compared with isolated silver nanoparticles, multimers exhibit more complex geometries and near-field distributions, making their forbidden-mode behavior an interesting case to study. Figure 5a presents the normalized forbidden-mode spectra for different nanoparticle structures, and Figure 5b shows the corresponding AFM images of trimers (particles 1–3), dimers (particles 4–6), and isolated (particles 7–9) nanoparticles. The spectra in Figure 5a demonstrate three typical activation behaviors: first, where all three forbidden modes are activated; second, where only E'' and E_{1g} are activated while A_2'' remains absent; and third, where all forbidden modes are either too weak or invisible. By comparing with the corresponding AFM morphologies, we observe that the activation of A_2'' is inversely correlated with nanoparticle height, whereas the activation of E'' and E_{1g} is inversely correlated with the lateral size of individual particles within the multimer. Although the correlations are less pronounced than in the isolated silver nanoparticle case due to the structural complexity, the directional size dependence is still clearly identifiable.

To further analyze the behavior of multimers, we performed electromagnetic simulations on typical dimer and trimer configurations. In the simulation, we used the same spherical nanoparticles with diameters of 80 nm as in the isolated silver nanoparticle simulations. Figure 5c-1,c-2, and (c-3) shows the near-field electric distributions under z-polarization illumination in the interfacial lateral plane between the sample and the nanoparticles of trimer, dimer, and isolated nanoparticle, respectively. These electric-field maps show that the fields generated by interparticle gaps in multimers do not affect the near-field distribution in the vicinity of the nanoparticle-MoS_2 interface. For nanoparticles with an average diameter of 80 nm, the interparticle gap centers are located about 40 nm above the nanoparticle-MoS_2 interface, so the gap-related near field or interparticle hotspot does not play a role in either Raman enhancement or forbidden-mode activation. The simulations also show that the number of nanoparticles in a dimer and trimer does not change the near-field gradient, but it does increase the overall near-field intensity due to the presence of multiple particles. This observation is consistent with the experimental results, in which the Raman-active modes exhibit greater enhancement in multimers than in isolated silver nanoparticles due to the overall increased near-field intensity. Therefore, the enhancement of the Raman-active modes already contains the contribution from the number of particles in a multimer. Once the spectra are normalized by these modes, the influence of the field enhancement and thus the number of particles is removed, causing the normalized forbidden-mode intensity to resemble that of individual nanoparticles. Because

the simulations show that each particle in trimers and dimers produces nearly the same near-field gradient regardless of the number of particles, the key factor determining forbidden-mode activation in multimers reduces back to the same factor as in isolated silver nanoparticles, where the individual particle size. Therefore, the forbidden-mode activation continues to follow the same principle: nanoparticle size determines near-field gradient strength, which in turn determines forbidden-mode activation efficiency.

Given this size-dependent trend, we also examined the extent to which physical deformation could contribute to the activation of the forbidden Raman modes. If the activation had a noticeable contribution from the deformation, larger nanoparticles or multimers with larger contact areas and stronger local strain should produce stronger forbidden Raman signals. However, our experimental results show the opposite trend: the normalized intensities of all forbidden modes decrease with increasing nanoparticle size. This behavior is consistent across all forbidden modes and is distinctly different from the enhancement trend observed in Raman-active modes. Therefore, the size dependence itself provides direct evidence against the deformation-dominated mechanism and clearly demonstrates that the key factor determining forbidden mode activation is the near-field gradient rather than the physical deformation induced by the nanoparticle. Combining the DFT calculations, spatial Raman imaging experiments, statistical size-dependent analysis, and electromagnetic simulations, we establish a clear and consistent mechanism for the activation of forbidden Raman modes.

3 | Conclusion

In this work, we developed a highly sensitive LF-PERS system and experimentally activated two kinds of low-frequency interlayer phonons, E'' and A_2'', that are normally forbidden by Raman selection rules in 3-layered MoS_2. Through DFT simulations, we confirmed that these forbidden modes are intrinsic vibrational modes of the material. A systematic analysis showed that the normalized intensity of the forbidden modes decreases markedly with increasing nanoparticle size. This trend was opposite to that of the enhancement effect governed by the near-field intensity, but was fully consistent with the decay of the near-field gradient. The same size-dependent behavior was observed in nanoparticle multimers. This size dependence ruled out the possibility of a deformation-dominated mechanism and demonstrated that the activation of forbidden modes is determined by the local near-field gradient, while physical deformation may contribute only a minor symmetry-relaxation effect. Therefore, the appearance of forbidden modes arose primarily from the additional optical momentum provided by the strong near-field gradient, with local deformation serving as a secondary factor that assists symmetry breaking. This work not only reveals the activation mechanism of hidden interlayer phonons in 2D materials but also establishes a new plasmonic near-field-based approach for probing forbidden phonons, interlayer interactions, and symmetry breaking.

Acknowledgements

The calculations were partly carried out using the supercomputers at the Research Center for Computational Science in Okazaki (Project: 23-IMS-C017, 24-IMS-C018, and 25-IMS-C019) and the Institute for Chemical Research, Kyoto University.

Funding

This work was partially supported by JST FOREST (JPMJFR233Z), JSPS Grant-in-Aid for Scientific Research (KAKENHI) (Grant in Aid for Scientific Research (B) JP24K01385, Grant-in-Aid for Transformative Research Areas (A) Publicly Offered Research "Chiral materials science pioneered by the helicity of light" JP25H01624, Grant-in-Aid for Transformative Research Areas (A) Publicly Offered Research "Materials science of meso-hierarchy" JP24H01717, Grant-in-Aid for Challenging Research (Exploratory) JP24K21718), and a research grant from the Takahashi Industrial and Economic Research Foundation.

Conflicts of Interest

The authors declare no conflicts of interest.

Data Availability Statement

The data that support the findings of this study are available on request from the corresponding author. The data are not publicly available due to privacy or ethical restrictions.

References

1. *Light Scattering in Solids I* (Springer, 1983), 366.

2. W. G. Fateley, N. T. McDevitt, and F. F. Bentley, "Infrared and Raman Selection Rules for Lattice Vibrations: The Correlation Method," *Applied Spectroscopy* 25, no. 2 (1971): 155–173, https://doi.org/10.1366/000370271779948600.

3. R. T. Sam, T. Umakoshi, and P. Verma, "Probing Stacking Configurations in a Few Layered MoS_2 by Low Frequency Raman Spectroscopy," *Scientific Reports* 10, no. 1 (2020): 21227, https://doi.org/10.1038/s41598-020-78238-w.

4. C. H. Lui, Z. Ye, C. Ji, et al., "Observation of Interlayer Phonon Modes in van der Waals Heterostructures," *Physical Review B* 91, no. 16 (2015): 165403, https://doi.org/10.1103/PhysRevB.91.165403.

5. X. Lu, M. I. B. Utama, J. Lin, et al., "Rapid and Nondestructive Identification of Polytypism and Stacking Sequences in Few-Layer Molybdenum Diselenide by Raman Spectroscopy," *Advanced Materials* 27, no. 30 (2015): 4502–4508, https://doi.org/10.1002/adma.201501086.

6. X. Ling, L. Liang, S. Huang, et al., "Low-Frequency Interlayer Breathing Modes in Few-Layer Black Phosphorus," *Nano Letters* 15, no. 6 (2015): 4080–4088, https://doi.org/10.1021/acs.nanolett.5b01117.

7. M. Liao, Z. Wei, L. Du, et al., "Precise Control Of The Interlayer Twist Angle In Large Scale MoS_2 Homostructures," *Nature Communications* 11, no. 1 (2020): 2153, https://doi.org/10.1038/s41467-020-16056-4.

8. L. Liang, J. Zhang, B. G. Sumpter, Q.-H. Tan, P.-H. Tan, and V. Meunier, "Low-Frequency Shear and Layer-Breathing Modes in Raman Scattering of Two-Dimensional Materials," *ACS Nano* 11, no. 12 (2017): 11777–11802, https://doi.org/10.1021/acsnano.7b06551.

9. S. Huang, L. Liang, X. Ling, et al., "Low-Frequency Interlayer Raman Modes to Probe Interface of Twisted Bilayer MoS 2," *Nano Letters* 16, no. 2 (2016): 1435–1444, https://doi.org/10.1021/acs.nanolett.5b05015.

10. J. Holler, S. Meier, M. Kempf, et al., "Low-frequency Raman scattering in WSe_2−$MoSe_2$ Heterobilayers: Evidence for Atomic Reconstruction," *Applied Physics Letters* 117, no. 1 (2020): 013104, https://doi.org/10.1063/5.0012249.

11. M. Boukhicha, M. Calandra, M.-A. Measson, O. Lancry, and A. Shukla, "Anharmonic Phonons in Few-Layer MoS_2: Raman Spectroscopy of Ultralow Energy Compression And Shear Modes," *Physical Review B* 87, no. 19 (2013): 195316, https://doi.org/10.1103/PhysRevB.87.195316.

12. C. Lee, H. Yan, L. E. Brus, T. F. Heinz, J. Hone, and S. Ryu, "Anomalous Lattice Vibrations of Single- and Few-Layer MoS_2," *ACS Nano* 4, no. 5 (2010): 2695–2700, https://doi.org/10.1021/nn1003937.

13. H. Zeng, B. Zhu, K. Liu, J. Fan, X. Cui, and Q. M. Zhang, "Low-frequency Raman Modes And Electronic Excitations In Atomically Thin MoS_2 Films," *Physical Review B* 86, no. 24 (2012): 241301, https://doi.org/10.1103/PhysRevB.86.241301.

14. Y. Saito, K. Takahiro, H. Ito, et al., "Low frequency Raman Study of Interlayer Couplings in WS_2–MoS_2 van der Waals Heterostructures," *Japanese Journal of Applied Physics* 59 (2020): 062004, https://doi.org/10.35848/1347-4065/ab9400.

15. K. Wang, B. Huang, M. Tian, et al., "Interlayer Coupling in Twisted WSe_2/WS_2 Bilayer Heterostructures Revealed by Optical Spectroscopy," *ACS Nano* 10, no. 7 (2016): 6612–6622, https://doi.org/10.1021/acsnano.6b01486.

16. A. A. Puretzky, L. Liang, X. Li, et al., "Low-Frequency Raman Fingerprints of Two-Dimensional Metal Dichalcogenide Layer Stacking Configurations," *ACS Nano* 9, no. 6 (2015): 6333–6342, https://doi.org/10.1021/acsnano.5b01884.

17. A. A. Puretzky, L. Liang, X. Li, et al., "Twisted $MoSe_2$ Bilayers With Variable Local Stacking and Interlayer Coupling Revealed by Low-Frequency Raman Spectroscopy," *ACS Nano* 10, no. 2 (2016): 2736–2744, https://doi.org/10.1021/acsnano.5b07807.

18. F. Liu, H. Liu, C. Chi, et al., "Giant Two-Photon Upconversion From 2D Exciton in Doubly-Resonant Plasmonic Nanocavity," *Light: Science & Applications* 14, no. 1 (2025): 312, https://doi.org/10.1038/s41377-025-02010-w.

19. L. G. Cançado, A. Jorio, E. H. M. Ferreira, et al., "Quantifying Defects in Graphene via Raman Spectroscopy at Different Excitation Energies," *Nano Letters* 11, no. 8 (2011): 3190–3196, https://doi.org/10.1021/nl201432g.

20. M. He, C. Ge, K. Braun, et al., "Room Temperature Fluorescence Blinking in MoS_2 Atomic Layers by Single Photon Energy Transfer," *Laser & Photonics Reviews* 16, no. 8 (2022): 2200144, https://doi.org/10.1002/lpor.202200144.

21. Z. Fang, S. Thongrattanasiri, A. Schlather, et al., "Gated Tunability and Hybridization of Localized Plasmons in Nanostructured Graphene," *ACS Nano* 7, no. 3 (2013): 2388–2395, https://doi.org/10.1021/nn3055835.

22. Y. Liu, Y. Zhao, F. Ye, et al., "Determining the Dipole Orientation of Second Harmonic Generation in 3R-MoS_2 for Enhanced Nonlinear Susceptibility," *ACS Nano* 19, no. 35 (2025): 31882–31893, https://doi.org/10.1021/acsnano.5c11386.

23. N. Scheuschner, R. Gillen, M. Staiger, and J. Maultzsch, "Interlayer Resonant Raman Modes in Few-Layer MoS_2," *Physical Review B* 91, no. 23 (2015): 235409, https://doi.org/10.1103/PhysRevB.91.235409.

24. X. Zhang, W. P. Han, J. B. Wu, et al., "Raman Spectroscopy of Shear and Layer Breathing Modes in Multilayer MoS_2," *Physical Review B* 87, no. 11 (2013): 115413, https://doi.org/10.1103/PhysRevB.87.115413.

25. K. Uetsuki, P. Verma, T. Yano, Y. Saito, T. Ichimura, and S. Kawata, "Experimental Identification of Chemical Effects in Surface Enhanced Raman Scattering of 4-Aminothiophenol," *Journal of Physical Chemistry C* 114, no. 16 (2010): 7515–7520, https://doi.org/10.1021/jp9114805.

26. Z.-X. Yan, Y.-L. Zhang, W. Wang, et al., "Superhydrophobic SERS Substrates Based on Silver-Coated Reduced Graphene Oxide Gratings Prepared by Two-Beam Laser Interference," *ACS Applied Materials & Interfaces* 7, no. 49 (2015): 27059–27065, https://doi.org/10.1021/acsami.5b09128.

27. M. Osawa, N. Matsuda, K. Yoshii, and I. Uchida, "Charge Transfer Resonance Raman Process In Surface-Enhanced Raman Scattering From p-Aminothiophenol Adsorbed on Silver: Herzberg-Teller Contribution," *Journal of Physical Chemistry* 98, no. 48 (1994): 12702–12707, https://doi.org/10.1021/j100099a038.

28. H. Xu, E. J. Bjerneld, M. Käll, and L. Börjesson, "Spectroscopy of Single Hemoglobin Molecules by Surface Enhanced Raman Scattering," *Physical Review Letters* 83, no. 21 (1999): 4357–4360, https://doi.org/10.1103/PhysRevLett.83.4357.

29. S. Nie and S. R. Emory, "Probing Single Molecules and Single Nanoparticles by Surface-Enhanced Raman Scattering," *Science* 275, no. 5303 (1997): 1102–1106, https://doi.org/10.1126/science.275.5303.1102.

30. K. Kneipp, Y. Wang, H. Kneipp, et al., "Single Molecule Detection Using Surface-Enhanced Raman Scattering (SERS)," *Physical Review Letters* 78, no. 9 (1997): 1667–1670, https://doi.org/10.1103/PhysRevLett.78.1667.

31. D.-K. Lim, K.-S. Jeon, H. M. Kim, J.-M. Nam, and Y. D. Suh, "Nanogap-engineerable Raman-Active Nanodumbbells for Single-Molecule Detection," *Nature Materials* 9, no. 1 (2010): 60–67, https://doi.org/10.1038/nmat2596.

32. K. E. Shafer-Peltier, C. L. Haynes, M. R. Glucksberg, and R. P. Van Duyne, "Toward a Glucose Biosensor Based on Surface-Enhanced Raman Scattering," *Journal of the American Chemical Society* 125, no. 2 (2003): 588–593, https://doi.org/10.1021/ja028255v.

33. X. Zhang, M. A. Young, O. Lyandres, and R. P. Van Duyne, "Rapid Detection of an Anthrax Biomarker by Surface-Enhanced Raman Spectroscopy," *Journal of the American Chemical Society* 127, no. 12 (2005): 4484–4489, https://doi.org/10.1021/ja043623b.

34. R. G. Freeman, K. C. Grabar, K. J. Allison, et al., "Self-Assembled Metal Colloid Monolayers: An Approach to SERS Substrates," *Science* 267, no. 5204 (1995): 1629–1632, https://doi.org/10.1126/science.267.5204.1629.

35. M. Moskovits, "Surface-enhanced Raman Spectroscopy: A Brief Retrospective," *Journal of Raman Spectroscopy* 36, no. 6-7 (2005): 485–496, https://doi.org/10.1002/jrs.1362.

36. K. Kneipp, A. Jorio, H. Kneipp, et al., "Polarization Effects In Surface-Enhanced Resonant Raman Scattering Of Single-Wall Carbon Nanotubes On Colloidal Silver Clusters," *Physical Review B* 63, no. 8 (2001): 081401, https://doi.org/10.1103/PhysRevB.63.081401.

37. M. Fleischmann, P. J. Hendra, and A. J. McQuillan, "Raman Spectra of Pyridine Adsorbed at a Silver Electrode," *Chemical Physics Letters* 26, no. 2 (1974): 163–166, https://doi.org/10.1016/0009-2614(74)85388-1.

38. E. J. Ayars, C. L. Jahncke, M. A. Paesler, and H. D. Hallen, "Fundamental differences Between micro- and nano-Raman spectroscopy," *Journal of Microscopy* 202, no. 1 (2001): 142–147, https://doi.org/10.1046/j.1365-2818.2001.00878.x.

39. K. Kneipp, H. Kneipp, I. Itzkan, R. R. Dasari, and M. S. Feld, "Ultrasensitive Chemical Analysis by Raman Spectroscopy," *Chemical Reviews* 99, no. 10 (1999): 2957–2976, https://doi.org/10.1021/cr980133r.

40. A. M. Polubotko, "Some anomalies of the SER spectra of symmetrical molecules adsorbed on transition metal substrates: Consideration by the dipole–quadrupole SERS theory," *Journal of Raman Spectroscopy* 36, no. 6-7 (2005): 522–532, https://doi.org/10.1002/jrs.1344.

41. P. Verma, "Tip-Enhanced Raman Spectroscopy: Technique and Recent Advances," *Chemical Reviews* 117, no. 9 (2017): 6447–6466, https://doi.org/10.1021/acs.chemrev.6b00821.

42. R. Kato, T. Umakoshi, R. T. Sam, and P. Verma, "Probing Nanoscale Defects And Wrinkles in MoS_2 by Tip-Enhanced Raman Spectroscopic Imaging," *Applied Physics Letters* 114, no. 7 (2019): 073105, https://doi.org/10.1063/1.5080255.

43. D. Mrđenović, Z.-F. Cai, Y. Pandey, G. L. Bartolomeo, R. Zenobi, and N. Kumar, "Nanoscale Chemical Analysis of 2D Molecular Materials Using tip-Enhanced Raman Spectroscopy," *Nanoscale* 15, no. 3 (2023): 963–974, https://doi.org/10.1039/D2NR05127C.

44. T. Hartman, C. S. Wondergem, N. Kumar, A. van den Berg, and B. M. Weckhuysen, "Surface- and Tip-Enhanced Raman Spectroscopy in Catalysis," *Journal of Physical Chemistry Letters* 7, no. 8 (2016): 1570–1584, https://doi.org/10.1021/acs.jpclett.6b00147.

45. J. Langer, D. Jimenez de Aberasturi, J. Aizpurua, et al., "Present and Future of Surface-Enhanced Raman Scattering," *ACS Nano* 14, no. 1 (2020): 28–117, https://doi.org/10.1021/acsnano.9b04224.

46. G.-H. Kim, J. Son, and J.-M. Nam, "Advances, Challenges, and Opportunities in Plasmonic Nanogap-Enhanced Raman Scattering With Nanoparticles," *ACS Nano* 19, no. 3 (2025): 2992–3007, https://doi.org/10.1021/acsnano.4c14557.

47. M. V. Balois-Oguchi, N. Hayazawa, S. Yasuda, et al., "Probing Strain and Doping Along a Graphene Wrinkle Using Tip-Enhanced Raman Spectroscopy," *Journal of Physical Chemistry C* 127, no. 12 (2023): 5982–5990, https://doi.org/10.1021/acs.jpcc.2c08529.

48. K. Ikeda, "Surface Mass Analysis Of Heterogeneous Reactions Using Low-Frequency Surface-Enhanced Raman Scattering," *Current Opinion in Electrochemistry* 41 (2023): 101355, https://doi.org/10.1016/j.coelec.2023.101355.

49. A. C. Gadelha, D. A. A. Ohlberg, C. Rabelo, et al., "Localization of Lattice Dynamics In Low-Angle Twisted Bilayer Graphene," *Nature* 590, no. 7846 (2021): 405–409, https://doi.org/10.1038/s41586-021-03252-5.

50. M. Kang, H. Kim, E. Oleiki, et al., "Conformational Heterogeneity of Molecules Physisorbed on a Gold Surface at Room Temperature," *Nature Communications* 13, no. 1 (2022): 4133, https://doi.org/10.1038/s41467-022-31576-x.

51. T. Moon, H. Joo, B. Das, et al., "Adaptive Gap-Tunable Surface-Enhanced Raman Spectroscopy," *Nano Letters* 24, no. 12 (2024): 3777–3784, https://doi.org/10.1021/acs.nanolett.4c00289.

52. M.-F. Cao, X.-H. Peng, X.-J. Zhao, et al., "Ultralow-Frequency Tip-Enhanced Raman Scattering Discovers Nanoscale Radial Breathing Mode on Strained 2D Semiconductors," *Advanced Materials* 36, no. 35 (2024): 2405433, https://doi.org/10.1002/adma.202405433.

53. M. Takase, H. Ajiki, Y. Mizumoto, et al., "Selection-rule Breakdown In Plasmon-Induced Electronic Excitation Of An Isolated Single-Walled Carbon Nanotube," *Nature Photonics* 7, no. 7 (2013): 550–554, https://doi.org/10.1038/nphoton.2013.129.

54. A. M. Polubotko, "Manifestation of Strong Quadrupole Light–Molecule Interaction in the SER and SEHR Spectra Of Pyrazine And Phenazine," *Chemical Physics Letters* 519-520 (2012): 110–117, https://doi.org/10.1016/j.cplett.2011.10.008.

55. S. Li, E. Drueke, Z. Porter, et al., "Symmetry-Resolved Two-Magnon Excitations in a Strong Spin-Orbit-Coupled Bilayer Antiferromagnet," *Physical Review Letters* 125, no. 8 (2020): 087202, https://doi.org/10.1103/PhysRevLett.125.087202.

56. K. Ikeda, M. Takase, N. Hayazawa, S. Kawata, K. Murakoshi, and K. Uosaki, "Plasmonically Nanoconfined Light Probing Invisible Phonon Modes in Defect-Free Graphene," *Journal of the American Chemical Society* 135, no. 31 (2013): 11489–11492, https://doi.org/10.1021/ja4056596.

57. E. J. Ayars, H. D. Hallen, and C. L. Jahncke, "Electric Field Gradient Effects in Raman Spectroscopy," *Physical Review Letters* 85, no. 19 (2000): 4180–4183, https://doi.org/10.1103/PhysRevLett.85.4180.

58. D. J. Arenas, L. V. Gasparov, W. Qiu, J. C. Nino, C. H. Patterson, and D. B. Tanner, "Raman Study Of Phonon Modes In Bismuth Pyrochlores," *Physical Review B* 82, no. 21 (2010): 214302, https://doi.org/10.1103/PhysRevB.82.214302.

59. M. Moskovits and D. P. DiLella, "Intense Quadrupole Transitions In The Spectra Of Molecules Near Metal Surfaces," *Journal of Chemical Physics* 77, no. 4 (1982): 1655–1660, https://doi.org/10.1063/1.444008.

60. L. Liang and V. Meunier, "First-Principles Raman Spectra of MoS_2, WS_2 and Their Heterostructures," *Nanoscale* 6, no. 10 (2014): 5394–5401, https://doi.org/10.1039/C3NR06906.

61. Y. Zhao, K. T. E. Chua, C. K. Gan, et al., "Phonons in Bi_2S_3 Nanostructures: Raman Scattering And First-Principles Studies," *Physical Review B* 84, no. 20 (2011): 205330, https://doi.org/10.1103/PhysRevB.84.205330.

62. J. Ribeiro-Soares, R. M. Almeida, E. B. Barros, et al., "Group Theory Analysis Of Phonons In Two-Dimensional Transition Metal Dichalcogenides," *Physical Review B* 90, no. 11 (2014): 115438, https://doi.org/10.1103/PhysRevB.90.115438.

63. S. B. Desai, S. R. Madhvapathy, M. Amani, et al., "Gold-Mediated Exfoliation of Ultralarge Optoelectronically-Perfect Monolayers," *Advanced Materials* 28, no. 21 (2016): 4053–4058, https://doi.org/10.1002/adma.201506171.

64. R. Kato, T. Moriyama, T. Umakoshi, T. Yano, and P. Verma, "Ultra-stable Tip-Enhanced Hyperspectral Optical Nanoimaging for Defect Analysis of Large-Sized WS_2 Layers," *Science Advances* 8, no. 28 (2022): abo4021, https://doi.org/10.1126/sciadv.abo4021.

65. A. Glebov, O. Mokhun, A. Rapaport, S. Vergnole, V. Smirnov, and L. Glebov, "Volume Bragg Gratings as Ultra-narrow and Multiband Optical Filters," *SPIE:* 8428 (2012): 84280C, https://doi.org/10.1117/12.923575.

66. T. Mino, Y. Saito, and P. Verma, "Quantitative Analysis of Polarization-Controlled Tip-Enhanced Raman Imaging Through the Evaluation of the Tip Dipole," *ACS Nano* 8, no. 10 (2014): 10187–10195, https://doi.org/10.1021/nn5031803.

67. T. Mino, Y. Saito, and P. Verma, "Control of Near-Field Polarizations For Nanoscale Molecular Orientational Imaging," *Applied Physics Letters* 109, no. 4 (2016): 041105, https://doi.org/10.1063/1.4960016.

68. A. Erba, J. K. Desmarais, S. Casassa, et al., "CRYSTAL23: A Program for Computational Solid State Physics and Chemistry," *Journal of Chemical Theory and Computation* 19, no. 20 (2023): 6891–6932, https://doi.org/10.1021/acs.jctc.2c00958.

69. F. Corà, A. Patel, N. M. Harrison, C. Roetti, A. Richard, and C. Catlow, "Anab initio Hartree–Fock study of α-MoO_3," *Journal of Materials Chemistry* 7, no. 6 (1997): 959–967, https://doi.org/10.1039/A607439A.

70. T. Ouazzani, A. Lichanot, C. Plsani, and C. Roetti, "Relaxation and Electronic Structure Of Surfaces In Lithium Sulphide: A Hartree-Fock ab Initio Approach," *Journal of Physics and Chemistry of Solids* 54, no. 11 (1993): 1603–1611, https://doi.org/10.1016/0022-3697(93)90356-V.

71. E. Aprà, E. Stefanovich, R. Dovesi, and C. Roetti, "An ab Initio Hartree—Fock Study Of Silver Chloride," *Chemical Physics Letters* 186, no. 4 (1991): 329–335, https://doi.org/10.1016/0009-2614(91)90187-E.

72. A. van de Walle and G. Ceder, "Correcting Overbinding In Local-Density-Approximation Calculations," *Physical Review B* 59, no. 23 (1999): 14992–15001, https://doi.org/10.1103/PhysRevB.59.14992.

73. J. M. Gonzalez and I. I. Oleynik, "Layer-Dependent Properties of SnS_2 and $SnSe_2$ Two-Dimensional Materials," *Physical Review B* 94, no. 12 (2016): 125443, https://doi.org/10.1103/PhysRevB.94.125443.

74. A. J. Cohen, P. Mori-Sánchez, and W. Yang, "Challenges for Density Functional Theory," *Chemical Reviews* 112, no. 1 (2012): 289–320, https://doi.org/10.1021/cr200107z.

Supporting Information

Additional supporting information can be found online in the Supporting Information section.

Supporting File: lpor71618-sup-0001-SuppMat.pdf.